Universiteit
Leiden
The Netherlands

# Coupled electronic and nuclear dynamics at interfaces of artificial photosynthesis devices

Haas, T. de

**Citation**

Haas, T. de. (2025, September 4). *Coupled electronic and nuclear dynamics at interfaces of artificial photosynthesis devices*. Ridderprint, Leiden. Retrieved from https://hdl.handle.net/1887/4259657

| | |
|---|---|
| Version: | Publisher's Version |
| License: | Licence agreement concerning inclusion of doctoral thesis in the Institutional Repository of the University of Leiden |
| Downloaded from: | https://hdl.handle.net/1887/4259657 |

**Note:** To cite this publication please use the final published version (if applicable).

# Chapter 6: Effects of Nuclear Motion on the Photoinduced Interfacial Charge Transfer Dynamics at a NiO/P1 Photocathode

**Quantum/Classical dynamics simulations** were employed to interpret transient absorption spectroscopy measurements on a push-pull dye absorbed on NiO.

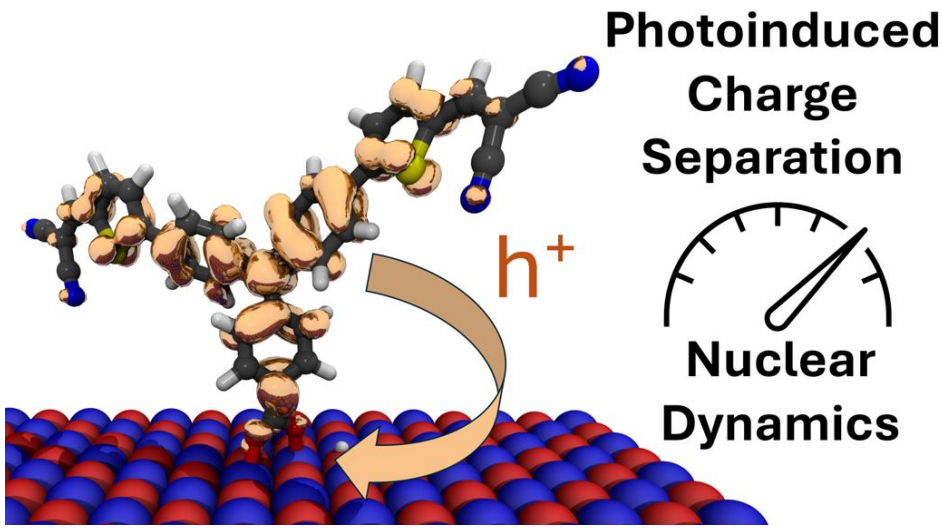


**This chapter is based on:**

T. de Haas*, K. Zhu*, J.M. van der Sterre, Y. Luo, G. Mul, F. Buda, A. Huijser. Effects of Nuclear Motion on the Photoinduced Interfacial Charge Transfer Dynamics at a NiO/P1 Photocathode. *J. Phys. Chem. C*. **2025**, *129* (14), 6817-6826 (* contributed equally)

## 6.1 Abstract

The performance of dye-sensitized photoelectrochemical cells is presently limited by the photocathode component. Here, we investigate the impact of nuclear dynamics on the photoinduced charge separation of the benchmark NiO/P1 system (P1 = 4-(bis-4-(5-(2,2-dicyano-vinyl)-thiophene-2-yl)-phenyl-amino)-benzoic acid). Transient absorption (TA) studies in aqueous environments with different viscosities show that photoinduced hole injection either proceeds ultrafast (<100 fs) or in a sub-ps time window. We assign the fastest component to a surface species strongly coupled to the NiO. Interestingly, the slower injection component and charge recombination are slowed down considerably in increasingly viscous media. Quantum-classical dynamics simulations of a system with the dye standing perpendicular to the surface yield an injection lifetime remarkably close to the slow component from kinetic modelling of the TA results. Simulations including nuclear thermal motion yield a two-fold increase in hole transfer rate compared to simulations for which the nuclei were fixed, highlighting the role of nuclear motion and providing new design principles for dye-sensitized photocathodes.

## 6.2 Introduction

The development of efficient solar conversion devices is essential to advance the energy transition. Dye-sensitized photoelectrochemical cells (DS-PEC) are attractive because of their tunable properties and capability to directly convert solar energy into $H_2$ through water splitting or into other fuels via $CO_2$ reduction.[1,2] In a typical DS-PEC cell, both photoanode and photocathode consist of a wide bandgap nanoporous semiconductor functionalized with light-absorbing dyes and catalysts. However, the efficiency of the photocathode is substantially lower than that of a photoanode,[3] limiting the overall performance of a DS-PEC and highlighting the importance of developing efficient photocathodes.

The choice for NiO as p-type semiconductor is motivated by its electronic energy levels and chemical stability.[4] Despite numerous efforts focused on the NiO nanostructure and doping, and the design of new dyes and catalysts,[5] improving the efficiency of NiO-based photocathodes remains a challenge. Hole injection from the photoexcited dye into the NiO typically occurs on a sub-ps timescale[6] and should be followed by electron transfer from the dye into the catalyst.[7] However, hole injection does not necessarily occur with close to unity quantum yield[8] and also detrimental charge recombination between dye radical anions and holes injected into the NiO occurs fast, typically in a ps-ns time window.[9] The photocathode performance is well known to depend on the NiO nanostructure,[10] doping,[7,9] and the chemical structures of the dye and catalyst.[7,11–17] Also the nature of the electrolyte and the composition of the electrochemical double layer play an important role in the performance and interfacial photodynamics.[18]

Theoretical studies by several groups on a variety of molecule-semiconductor photoanode systems have emphasized the key role of the nuclear dynamics in the interfacial photodynamics.[19–21] These studies highlight that nuclear motion can facilitate non-adiabatic charge transfer channels which dominate the injection process when the electronic coupling between donor and acceptor moieties is low. Prezhdo *et al.* studied Ru complexes chemisorbed onto $Ta_2O_5$, either via COOH or $PO_3H_2$ anchoring groups. Non-adiabatic quantum-classical molecular dynamics

(MD) simulations based on Extended Hückel (EH) theory indicate that photoinduced electron transfer from the Ru complex into $Ta_2O_5$ is faster with COOH anchoring groups than for the same complex with $PO_3H_2$ anchoring groups, due to a stronger non-adiabatic coupling for the COOH anchored complex. The COOH anchoring groups promote charge transfer with higher frequency vibrational modes than the $PO_3H_2$ anchoring groups. Quantum decoherence appears to counteract this effect to a small extent, because of a faster decay in the COOH-anchored system compared to the $PO_3H_2$ tethering.[22] Monti *et al.* studied the interfacial photoinduced electron transfer for a terrylene dye anchored on $TiO_2$ by a phenyl-amide-phenyl molecular rectifier bridge. They found that the inclusion of nuclear dynamics is crucial to observe the process, and the electron propagation shows oscillatory features that correlate with interatomic distance fluctuations in the bridge.[23] Similarly, Torres and co-workers have investigated a $TiO_2$ surface sensitized with a perylene dye and observed that nuclear motion couples to the electron wave packet propagation.[19] The role of nuclear-electronic coupling in intramolecular charge transfer has also been studied extensively for ruthenium-based dye compounds. These works have shown through both experimental and computational methods that specific molecular vibrations can couple to electron and hole dynamics in such systems.[24–27]

The photosensitization of NiO can be achieved with various dye's and has been studied extensively in the context of dye-sensitized solar cells.[28] Particularly interesting is a class dyes consisting of π-conjugated donor (D) and acceptor (A) moieties, commonly referred to as D-A dyes. Photoexcitation in these complexes is associated with a donor-to-acceptor electron transfer, resulting in a spatial separation of the electron-hole pair, which helps prevent charge recombination. In a previous publication, we have demonstrated that this electron transfer can cause the acceptor moiety of the dye to twist relative to the donor moiety.[29]

In the present work, we explore the photoinduced hole injection and charge recombination dynamics in a benchmark D-A dye chemisorbed on NiO. In

particular, the role of nuclear motion on the photoinduced interfacial dynamics is investigated by combining EH-based quantum-classical dynamics simulations with femtosecond transient absorption studies in aqueous environments with different viscosities. The NiO is functionalized with the D-A dye P1 [4-(bis-4-(5-(2,2-dicyano-vinyl)-thiophene-2-yl)-phenyl-amino)-benzoic acid] by chemisorption via the COOH anchoring group. The P1 dye combines a triphenylamine donor unit linked via thiophene bridges to two dicyanovinylene acceptors. We observe that photoinduced hole injection either proceeds on an ultrafast timescale, during which the process is driven by electronic coupling, or in a sub-ps time window where nuclear motion is critical for the injection process. Especially the fluctuations in the dihedrals between the donor and acceptor moieties of the dye, and fluctuations in the carboxylate O – surface Ni distance appears to be important for photoinduced hole injection, although other nuclear dynamics likely play a role as well. Also charge recombination depends on the structural dynamics and slows down in viscous media. Our work highlights the importance of understanding the interplay between nuclear dynamics and photoinduced charge separation and recombination, which is essential for the development of photocathodes where structural flexibility is tailored for efficient solar to fuel conversion.

## 6.3 Methods

### *6.3.1 Sample preparation and transient absorption experiments*

The sample preparation and femtosecond transient absorption setup has been described in detail earlier.[9] Polyethylene glycol (PEG) was purchased from Sigma Aldrich (BioUltra, 1000, $M_n$ 950-1050) and dissolved into MilliQ water with a concentration of 4.5 wt%.

### *6.3.2 Computational Methods*

Multiple computational methodologies were combined to study the electronic and structural factors that govern interfacial hole-transfer dynamics between the

photoexcited dye P1* and the NiO surface. A schematic overview of the employed computational workflow is provided in Scheme 1. Density functional theory (DFT) was used to optimize both the geometries and electronic structure of P1 and the NiO semiconductor slab (details provided in the Appendix, A1, A2 and A7). The obtained dye and slab structures were used to build the configurations discussed in section 6.4.4. Then, nuclear classical dynamics simulations were performed of the dye molecule on the fixed DFT-optimized NiO using the self-consistent GFN-xTB tight-binding Hamiltonian.[30] We note that these simulations did not include explicit solvent. The Coulomb integral parameters of the employed EH model were optimized to reproduce the energy level alignment of the NiO/P1 interface, while that the spatial distribution of the P1 HOMO and LUMO orbitals closely matched the DFT results. This optimization procedure targetted the NiO band gap, the P1 HOMO-LUMO gap and the relative alignment of the P1 HOMO with the NiO valence band maximum (VBM), as discussed further in section 6.3.2.1. Details on the EH parameter optimization are provided in the Appendix, section 6A.8. Finally, the photoexcited electron and hole wave packet quantum dynamics were propagated either on a static nuclear geometry or on a precomputed nuclear trajectory using an EH approach. We have used a similar strategy based on semi-empirical calculations in earlier work to describe photoinduced electron transfer dynamics in a dye-$TiO_2$ interface.[21] The details of the wave packet propagation schemes are explained in the papers by Rego and Batista.[31,32] Details on the applied computational methodologies are provided in the Appendix, sections 6A.1-6A.4.

*Scheme 6.1. Schematic overview of the workflow used for photoinduced hole injection simulations on the P1/NiO system. VMB = valence band maximum, MD = molecular dynamics, EH = Extended Hückel.*

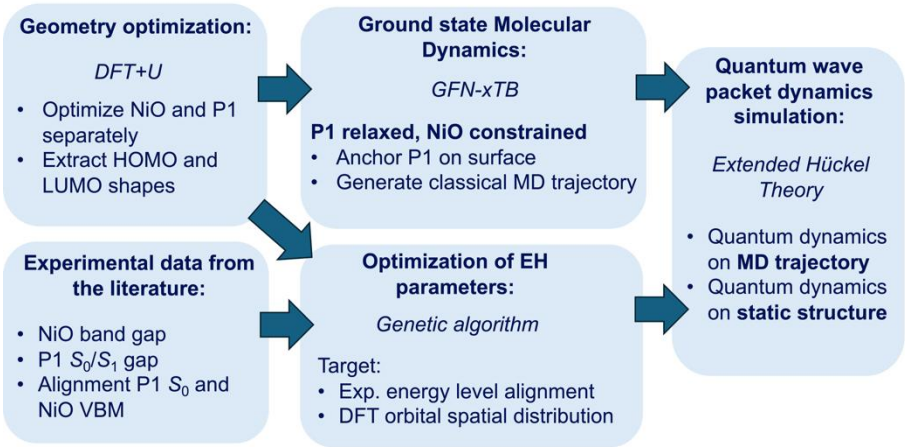


## 6.4 Results

### *6.4.1 Femtosecond transient absorption results*

To investigate the effect of nuclear dynamics on photoinduced charge separation and recombination, femtosecond transient absorption (TA) studies have been carried out using 500 nm pump pulses, predominantly exciting the π-π* transition of the P1 dyes.[13] We compared the photodynamics of NiO/P1 in $H_2O$ and NiO/P1 in $H_2O$ with 4.5 wt% polyethylene glycol (PEG), with the latter increasing the viscosity of the solvent and, therefore, likely slowing down the nuclear dynamics of the P1 molecule. Anchoring of the P1 dye onto the NiO surface via its COOH group causes deprotonation.[33,34] The P1 molecules are solvated by $H_2O$ and PEG molecules, and $H_2O$ molecules are likely adsorbed onto the NiO surface.[18] Dissociative $H_2O$ adsorption onto NiO has been reported to result in the formation of various Ni-OH surface species.[35]

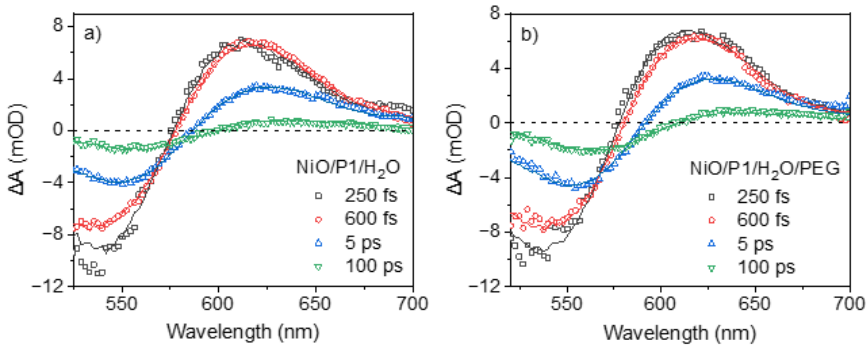


***Figure 6.1.*** *TA spectra for NiO/P1/$H_2O$ (a) and NiO/P1/$H_2O$/PEG (b) at selected time delays after 500 nm excitation. The solid lines indicate fits from target analysis.*

Figure 6.1 shows the TA spectra at various time delays for NiO/P1 in $H_2O$ (a) and in $H_2O$/PEG (b) and fits from photophysical modelling (see below). All spectra show a negative signal below *ca.* 600 nm due to ground state bleach (GSB) of the photoexcited P1 dye (P1*). Also stimulated emission (SE) by P1* may contribute to the early-time negative TA signal. Tian and co-workers observed SE at around 660 nm.[6] Fluorescence up-conversion studies by Gustavsson *et al*. showed a signal at around 600 nm, decaying on a sub-ps time scale due to electronic relaxation from the bright Franck-Condon state into a low-emitting charge-transfer state.[36] The positive TA signal around 610 nm at early times and red-shifting in time towards *ca.* 635 nm can be assigned to four distinct species. The first two are related to the dye: P1* has an absorption band centered around 550 nm and the P1 radical anion ($P1^{\bullet-}$) formed after hole injection into the NiO around 615 nm.[12,13] The other two are due to redox processes in the NiO induced by photoinduced hole injection, resulting in $Ni^{3+}$ and $Ni^{4+}$ centres contributing to the absorption above 650 nm.[37] Photoinduced hole injection by P1* resulting in $P1^{\bullet-}$ formation occuring beyond the TA time resolution (100-150 fs) contributes to the

red-shift in TA spectrum with time observed here. The TA signals decay on a ps-ns time scale due to charge recombination.

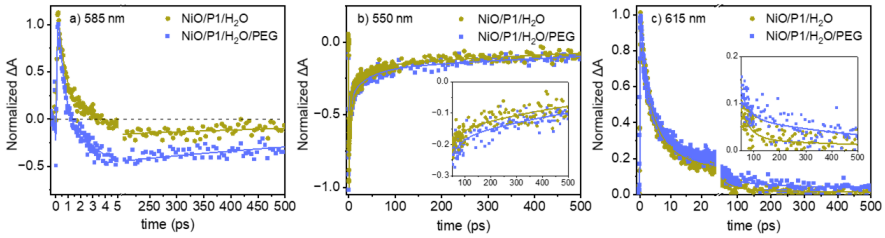


***Figure 6.2.*** *Normalized TA kinetic traces following 500 nm excitation for NiO/P1/H₂O and NiO/P1/H₂O/PEG at 585 nm (a), 550 nm (b) and 615 nm (c). The solid lines indicate fits from target analysis.*

Figure 6.2a shows the early-time normalized TA kinetic traces at 585 nm of NiO/P1 in $H_2O$ and $H_2O$/PEG. The P1* signal at this wavelength persisting until a few ps exceeds that of the GSB&SE, resulting in a positive overall TA signal at early times. The signal decays faster in $H_2O$/PEG, suggesting a shorter P1* lifetime caused by faster hole injection. Figure 6.2 also compares the kinetic traces at 550 nm (b) and 615 nm (c) of NiO/P1 in $H_2O$ and in $H_2O$/PEG. The signal at 550 nm beyond a few ps is dominated by GSB, which is indicative of charge recombination and seems to decay slightly slower in $H_2O$/PEG. This difference is clear at *e.g.* 615 nm, which signal is predominantly due to $P1^{\bullet-}$. These observations are consistent with our photophysical modeling discussed below.

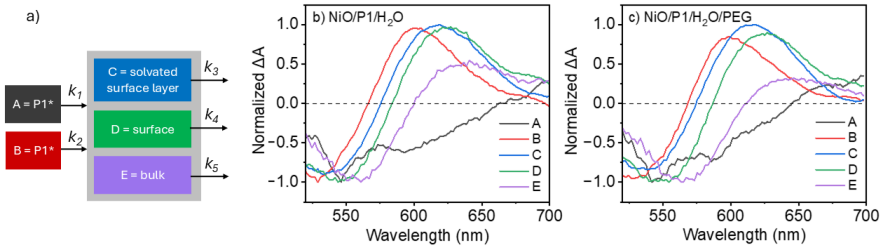


***Figure 6.3.*** *Photophysical model used for target analysis of the TA data (a) and obtained species associated spectra (SAS) for NiO/P1/$H_2O$ (b) and NiO/P1/$H_2O$/PEG (c).*

We performed target analysis using the program Glotaran.[38] Figure 6.3a presents a photophysical model based on five components that explains the TA data well. Photoinduced hole injection by P1* into the NiO either occurs ultrafast with rate constant $k_1$ or proceeds on a sub-ps time scale with rate constant $k_2$. Species A is a result of P1* GSB, SE and absorption, with GSB and especially SE dominating the TA signal. In contrast, species B does not show such strong SE contribution, consistent with the work of Gustavsson *et al.* with the fluorescence of P1* not only being quenched due to hole injection into NiO, but also by intrinsic sub-ps electronic relaxation from the bright Franck-Condon state into a low-emitting charge-transfer state observed for P1 on insulating $Al_2O_3$.[36] The time constants (Table 6.1, $\tau_x = 1/k_x$) qualitatively agree with the time constants obtained from quantum-classical dynamics simulations presented in the next section 6.4.4. The species associated spectra for each component are shown in Figures 6.3b and 6.3c. $\tau_1$ is slightly shortened in the presence of PEG, consistent with the faster decay shown in Figure 6.2a. Although the difference is small, it might be a result of a favourable initial P1 geometry for photoinduced hole injection induced by the PEG. In contrast to $\tau_1$, the value for $\tau_2$ is higher in $H_2O$/PEG compared to $H_2O$. We attribute this difference to the higher solvent viscosity in the presence of PEG, which likely slows down the nuclear dynamics of the P1 dye. Slow nuclear

dynamics delays hole injection, as is demonstrated in the quantum-classical dynamics simulations presented in the section 6.4.4.

To properly describe charge carrier recombination, at least three components are needed to get a good fit. The fastest component ($k_3$) is assigned to charge recombination between $P1^{\bullet-}$ and holes still present in the solvated NiO surface layer, the intermediate component ($k_4$) to recombination with holes at the NiO surface and the slowest component ($k_5$) to recombination with holes that have succeeded to escape into the NiO bulk. The spectra of the corresponding species C-E are included in Figures 6.3b and 6.3c and are clearly red-shifted relative to that of species B as a result of charge separation. Charge recombination is slightly slowed down in the presence of PEG, as also evident from Figure 6.2c, likely because of slow nuclear dynamics of the P1 dye due to the higher viscosity of $H_2O$/PEG compared to $H_2O$.

**Table 6.1.** Time scales obtained from target analysis.

| | NiO/P1 in $H_2O$ | NiO/P1 in $H_2O$/PEG |
|---|---|---|
| $\tau_1$ (fs) | 76 ± 3 | 60 ± 3 |
| $\tau_2$ (fs) | 479 ± 13 | 506 ± 12 |
| $\tau_3$ (ps) | 3.6 ± 0.04 | 3.9 ± 0.09 |
| $\tau_4$ (ps) | 33.3 ± 0.7 | 37.9 ± 0.7 |
| $\tau_5$ (ps) | 628.5 ± 15 | 725.5 ± 14 |

### *6.4.2 Quantum chemical modeling*

Motivated by the two chemical species identified through kinetic modeling of the TA results, we considered two configurations of P1 in our quantum chemical modeling studies. In the first configuration (species 1), the dye is oriented perpendicular to the surface, while in the second (species 2), P1 lies flat with both tails physisorbed to the surface. Visual representations of these two P1

configurations are shown in Figures 6.4a and 6.4b. DFT-based geometry optimizations, performed on a small representative model system, indicate that species 2 represents a local minimum on the dye-NiO potential energy surface. In vacuum, this configuration is ~30 kcal $mol^{-1}$ lower in energy than the perpendicular configuration (see Appendix section 6A.6, Table 6A.2). The stability of the flat configuration arises from a strong π-stacking interaction between the aniline rings of the model dye and the NiO surface. Although this stabilizing interaction is expected to be significantly reduced in the solvated system due to the saturation of Ni atoms with physisorbed water molecules, these calculations suggest that strong interactions between the surface layer and the P1 tails are likely. We have also performed DFT-based MD on the same model with explicit solvent at room temperature, which show that the dye remains standing perpendicular to the surface on the ps time scale (see Appendix, section 6A.6). Overall, we conclude that both species are likely to coexist on the surface. In both configurations, the carboxylate group is attached to the surface via a bidentate binding mode, with the COOH deprotonated and the excess proton bonded to an oxygen atom on the NiO surface. DFT studies of a similar dye with a carboxylate anchoring group have shown that this is the preferred binding mode on NiO (100).[33,34]

### *6.4.3 Electronic structure of the NiO/P1 interface*

The quantum wave packet dynamics is described by a semi-empirical EH Hamiltonian.[39,40] Prior to performing calculations, the parameters of this model were fine-tuned to reproduce the correct energy level alignment on the interface structure.[41] The HOMO orbital of the P1 has been estimated to be at ≈1.4 V vs NHE and the valence band maximum (VBM) for bulk NiO is found to be at ≈0.5 V vs NHE, providing a driving force of ≈0.9 V for hole injection by the photoexcited dye $P1^*$.[42,43] The 0-0 absorption of this dye has been estimated to be 2.24 eV, based on the intersection of absorption and emission spectra in

acetonitrile.[44] Bulk NiO has a band gap in the range of 3.4-4.3 eV, with the value depending on the measurement technique and the preparation method.[45–50] These values have been employed to define optimization targets for the bulk NiO band gap and for the P1 HOMO and LUMO orbital energies. A genetic algorithm was used to fine-tune the Coulomb integral parameters of the EH model, producing the correct energetic alignment, while simultaneously maintaining the proper symmetry and spatial distribution of the P1 HOMO and LUMO.[23] The details of the parametrization procedure are provided in section 6A.8.

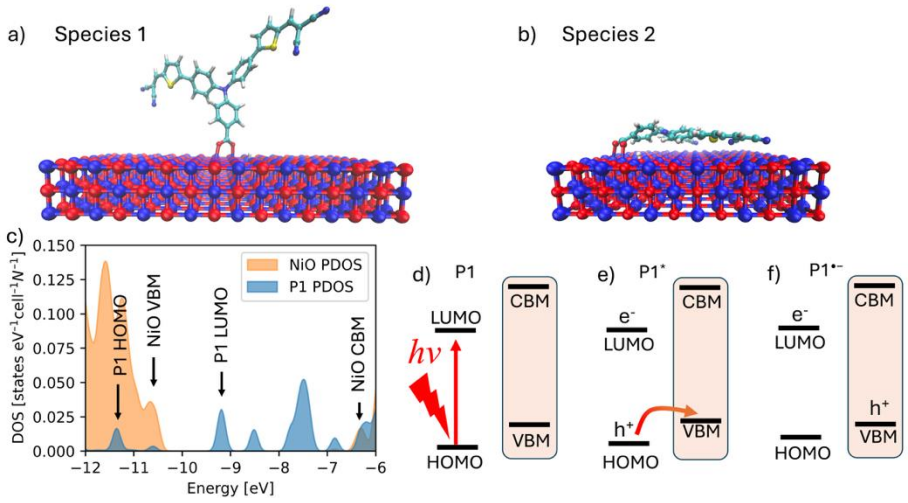


***Figure 6.4***. *Visualizations of the P1 dye in the two configurations considered: a) Species 1, standing perpendicular to the surface and b) Species 2, lying flat on the surface. c) Plot of the electronic density of states (DOS) of the optimized P1 dye on the NiO (100) slab, Species 1. The arrows indicate the positions of the P1 HOMO and LUMO orbitals and the NiO valence band maximum (VBM) and conduction band minimum (CBM) edges. The projected DOS (PDOS) of P1 and NiO were normalized by their respective number of atoms, N. d-f) Schematic overview of the investigated P1 excitation and subsequent hole injection process.*

Figure 6.4c shows the electronic density of states (DOS) obtained from the EH calculation on the NiO/P1 interface for species 1 shown in Figure 6.4a. The same DOS plot for species 2 can be found in the Appendix, Figure 6A.10 and shows qualitatively the same energy level alignment. The model predicts a NiO band gap of *ca.* 3.9 eV, consistent with experimental data. Furthermore, it shows that the P1 HOMO is 0.9 eV below the NiO valence band maximum (VBM) and the P1 LUMO is 2.2 eV above the P1 HOMO. It should be kept in mind that despite the correct energy level alignment, the model does not reproduce the anti-ferromagnetic alignment of the Ni d-electrons and is, therefore, not able to reproduce the consequential anisotropy in the quantum wave packet dynamics in the semiconductor. However, this model should give a sufficient description of the electronic structure, as our primary focus is elucidating the effects of the P1 structural motions on the photoinduced hole injection rate rather than the diffusion of the wave packet inside the semiconductor itself. We note that despite neglecting the spin, the opening of the NiO band gap was naturally reproduced with the default parameters.[41] Figure 6.4(d-f) provide a schematic overview of the hole injection simulations discussed in this work. Initially, the ground state P1 dye is exposed to a light flash (Figure 6.4d), which excites the system to the first electronic excited state (Figure 6.4e). This excited state is subsequently quenched by hole transfer from $P1^{*}$ to NiO, forming the reduced dye radical anion $P1^{\bullet-}$ (Figure 6.4f).

### *6.4.4 Hole injection simulations*

After optimizing and equilibrating P1 in the configuration standing perpendicular to the surface (see Figure 6.4a, species 1), a 3 ps ground state MD simulation of the dye was performed at the GFN-xTB level. The obtained trajectory was then divided into three sub-trajectories of equal length. Two EH based quantum dynamics simulations were performed on each sub-trajectory: the first simulation incorporated nuclear motion from the MD, while the second simulation was

performed using only the first MD snapshot as a static structure. By comparing these two simulations, the effect of thermal nuclear motion on the interfacial charge transfer dynamics was analyzed. Additionally, a single photoinduced hole injection simulation was performed on the optimized system where the dye lies flat on the surface (see Figure 6.4b, species 2). As the injection process for this species occurred on an ultrafast timescale, this simulation was carried out without including thermal nuclear motion.

Figure 6.5a presents the averaged hole survival probability (SP) for the species 1 photoexcited dye $P1^*$ over time, computed on the dynamic trajectories (blue) and on static structures (orange). Figure 6.5b presents the hole SP for the dye lying flat on the surface, while Figure 6.5c provides the injection traces for the individual trajectories of species 1, without averaging. The electron SP traces are provided in the Appendix, Figure 6A.4. Figures 6.5d and 6.5e display the hole density in Run 2 before and after injection. It is clearly observed that the hole is localized in the P1 HOMO orbital prior to injection, while it is delocalized over the entire NiO surface after injection.

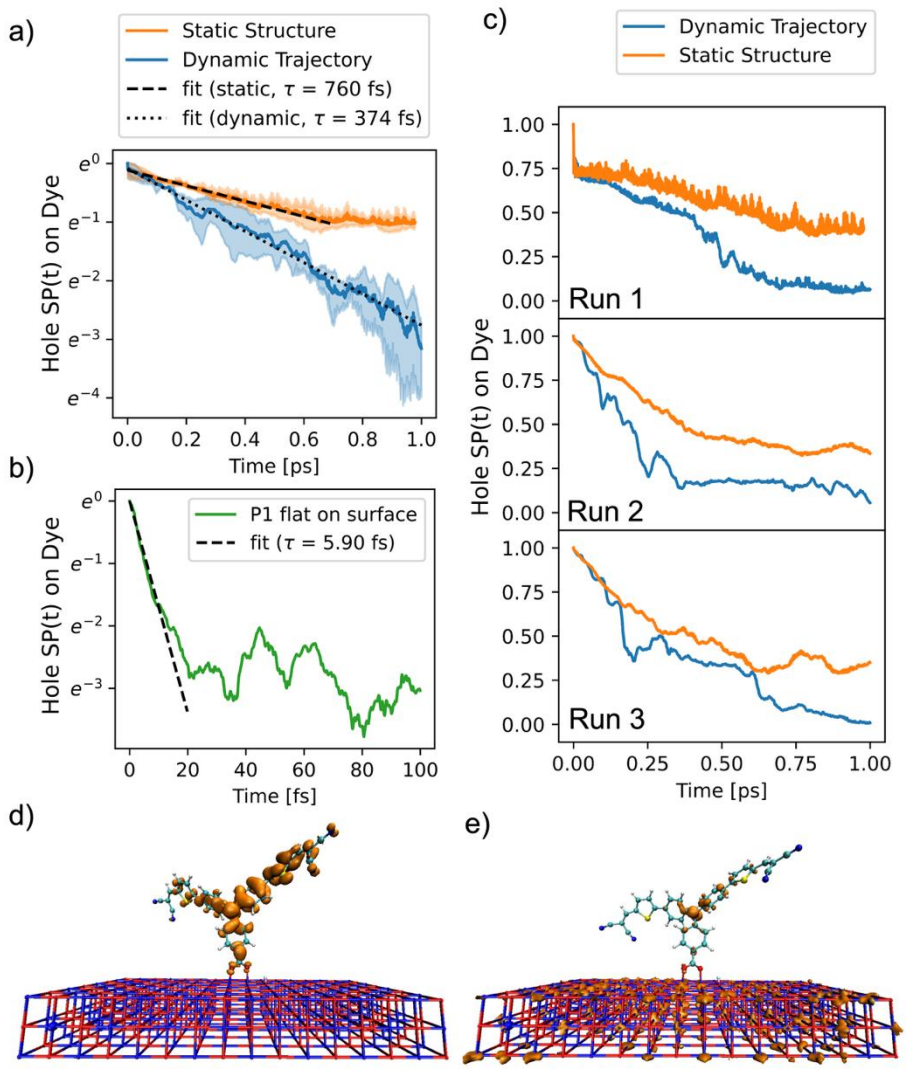


***Figure 6.5.*** *a) Time-dependent survival probability (SP) of the hole density on the excited dye P1* averaged over static structures (red) or dynamic trajectories (blue) for species 1. The transparent areas represent one standard deviation centered around the mean value. Panel b) shows the ultrafast injection in the case of species 2. Panel c) provides the traces of the individual runs for species 1 on a linear y-axis scale. Panels d) and e) present visualizations of the hole wave packet density at 0 and 900 fs extracted from Run 2.*

The averaged decay traces of the hole SP were modeled with an exponential decay function $m \cdot exp\left[\frac{-x}{\tau}\right]$. The $m$ parameter was introduced to account for the initial ultrafast injection on the first *ca.* 5 fs observed in Figure 6.5c, Run1. For P1 standing on the surface, this yielded lifetimes of 760 fs for the injection process on the fixed nuclei and 374 fs for the injection on the moving nuclei. This lifetime is remarkably close to the lifetime obtained for the second component by target analysis of the TA results (see Table 6.1). The fit for the injection on fixed nuclei was performed only on the first 690 fs, as the curve does not follow exponential behavior over the final 310 fs. Figures 6.5a and 6.5c highlight the critical role of nuclear dynamics on photoinduced hole injection in this system. Although all simulations predict a rapid initial injection process, the hole transfer rate on the static structures is rapidly diminished after approximately 66% of the charge density has been injected, resulting in an average SP on the dye of 34% after 1 ps. In contrast, the hole injection along the dynamic trajectories continues without stagnation during the 1 ps simulation, resulting in a 4% hole SP on the dye.

The first injection simulation with P1 standing on the surface (Run 1, Figure 5c) displays a remarkably fast initial injection, causing a 27 % reduction of hole SP on the P1 dye within the first 5 fs. This ultrafast component is attributed to very rapid hole transfer to an electronic orbital which is partly delocalized on the NiO (see Appendix, section 6A.10, Figure 6A.5). It was found that for the initial structure of Run 1, and other nuclear geometries, this orbital energy becomes nearly degenerate with the P1 HOMO energy ($E_{HOMO} - E_{HOMO-1} \approx 0.05$ eV, see Appendix, Figure 6A.5). The strong electronic coupling between these quasi-degenerate orbitals leads to an ultrafast charge transfer channel from the P1 HOMO to the NiO valence band.

Figure 6.5b presents the photo-induced hole-injection trace for the dye lying flat on the NiO surface. The charge transfer process for this species is observed to occur on a significantly faster timescale, with a sub-10 fs lifetime, which is nearly

two orders of magnitude shorter than that of the P1 oriented perpendicular to the surface. This much faster injection process occurs because the hole density can diffuse directly from the P1 aniline core into the NiO surface, without evolving through the carboxylate anchoring group.

We now further investigate the role of thermal nuclear motion on the interfacial charge transfer dynamics, specifically for species 1, where the dye stands perpendicular to the surface. To analyze this effect, we look at the hole SP trace in the frequency domain. By Fourier transforming the velocity autocorrelation function of the SP time evolution, power spectra were obtained for the hole SP on fixed and moving nuclei. Similarly, a vibrational density of states (VDOS) was obtained from the nuclear trajectory.

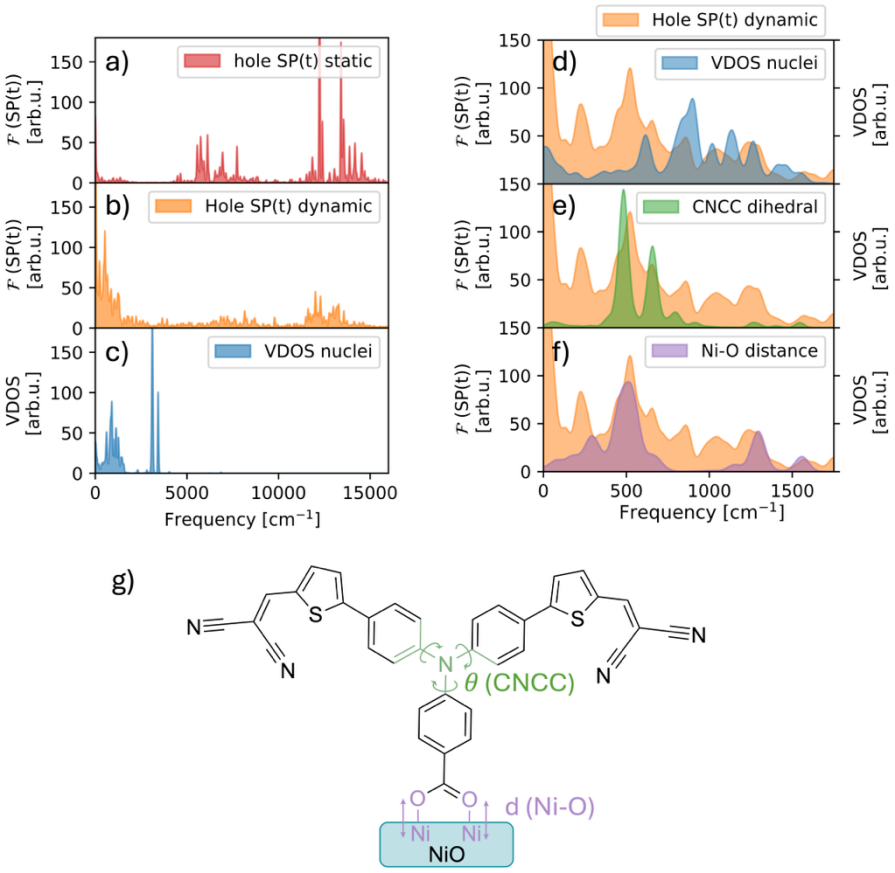


***Figure 6.6.*** *Frequency spectra associated with the hole transfer on fixed (a) and moving (b) nuclei, and the vibrational density of states (VDOS) of the nuclear trajectory (c). A frequency spectrum was computed for each run individually and subsequently averaged to obtain the displayed figure. Panel d) provides an overlay of hole SP frequency spectrum on moving nuclei and the VDOS of the entire trajectory. Additional overlays are provided for the same hole injection spectrum but now compared with the VDOS computed by considering only the CNCC dihedral angle torsions (e) or the Ni-O distance (f) fluctuations. The relevant Ni-O distances and CNCC dihedral angles are shown in panel g). Spectra for both Ni-O fluctuations and all three CNCC dihedral torsions (displayed in g) were averaged to produce the spectra displayed in e) and f).*

Figure 6.6a shows the hole injection frequency spectrum for the quantum dynamics performed on the static structures of species 1. The spectrum is characterized by sharp peaks around 6000 $cm^{-1}$, 12000 $cm^{-1}$ and 13500 $cm^{-1}$. These frequencies are associated with fast Rabi oscillations of the hole wave packet between different electronic eigenstates mostly located on the P1 dye, but with a slightly different delocalization on the NiO slab. Such rapid Rabi oscillations were also observed in the simulations by Torres *et al.*[19] Interestingly, the frequency spectrum of the injection trace on moving nuclei (Figure 6.6b) shows a much stronger signal in the 0-1700 $cm^{-1}$ region. As evidenced by the vibrational density of states (Figure 6.6c), this is precisely the frequency range where nuclear vibrations are expected to play a role. Evidently, the propagation of the hole wave packet exhibits strong coupling to the nuclear motion in this range. In figure 6.6d, the VDOS and hole SP frequency spectra are overlayed in the 0-1700 $cm^{-1}$ region. The frequency spectrum of the hole injection peaks around 500 $cm^{-1}$ and also contains several other characteristic frequencies. This observation indicates that a broad range of vibrations couple to the wave packet dynamics. To further investigate which vibrational modes are important, we extracted from the simulations the characteristic frequencies of specific geometrical features and found two modes that appear to be in resonance with the hole dynamics. Particularly, fluctuations of the CNCC dihedral angles (displayed in green in Figure 6.6g) and of the anchoring Ni-O distances (displayed in purple in Figure 6.6g) show high correlations with the injection process as evidenced by the spectra shown in Figure 6.6e and Figure 6.6f.

The influence of the CNCC dihedral angle on hole injection was further examined by visualizing the hole wave packet dynamics in the excited $P1^*$. A video (supplied in the associated content of the publication by de Haas *et al.*[51]), shows that the wave packet oscillates several times between the two tails of the $P1^*$ before eventually diffusing into the NiO surface. This behavior suggests that the specific geometric conformation of the dihedral angles at the P1 aniline core plays a

critical role in directing the wave packet. Depending on the alignment of these dihedrals, the wave packet may either evolve towards the surface or remain confined to the opposite tail. Recent studies on ruthenium bipyridine dye complexes show that, upon photoexcitation, electron transfer dynamics between the two bipyridine ligands can occur on a similar sub-100 fs timescale as observed here.[25]

## 6.5 Discussion

Quantum-classical dynamics simulations and femtosecond TA spectroscopy experiments were performed to investigate the photoinduced hole injection dynamics at the NiO/P1 interface, which serves as a benchmark system for photocathodes. After excitation of the P1 π-π* transition using 500 nm pump pulses, the excited dye P1* is quenched by rapid (sub-ps) hole injection into the valence band of NiO. Target analysis of the femtosecond TA data indicates that the photoinduced hole injection process in water is best described by a biexponential decay with lifetimes $\tau_1$ and $\tau_2$ of 76 ± 3 fs and 479 ± 13 fs, respectively. A good model for the subsequent charge carrier recombination process was obtained using three components with lifetimes of a few to several hundred picoseconds. The addition of PEG increases the values of $\tau_2$ - $\tau_5$, which could be attributed to slower nuclear dynamics of the P1 dye.

Motivated by the observation of two characteristic lifetimes for hole injection in the TA results, two systems were considered in our quantum chemical modelling studies. While in the first system, the P1 dye stands perpendicular to the surface (see Figure 6.4a), the second system considers the dye as it lies flat on the surface (see Figure 6.4b). DFT calculations on a smaller model system confirm that the dye is flexible and could form strong π-stacking interactions with the NiO surface. Although this suggests that the P1 dye could adopt configurations in which the tails come near the surface, the real system probably does not collapse to the surface entirely due to the solvating effect of surrounding water molecules and

due to the entropic gain associated with dissociation of the P1 tail from the surface. We attribute the fast component observed in the TA target analysis to a surface species in which the P1 aniline core is strongly coupled to the NiO surface layer. Quantum-classical dynamics simulations show that a P1 molecule that lies flat on the NiO surface exhibits a hole injection process characterized by a sub-10 fs lifetime. For the system with the dye standing on the surface, we observed that in specific geometric conformations, the electronic state corresponding to the hole occupying the P1 HOMO, becomes nearly degenerate with a state where the hole is delocalized on the P1 carboxylate bridge and the NiO surface. It was found that this quasi-degeneracy also leads to strong coupling between the $P1^*$ and the surface, providing a channel for ultrafast injection of roughly 27% of the hole density in ~5 fs.

Exponential fitting of the photoinduced hole injection trace for the P1 dye standing perpendicular to the surface yielded a characteristic lifetime of 374 fs, in near-quantitative agreement with the slower component of the injection in $H_2O$ media. The 22% faster decay in the simulation compared to the TA results is within the error margin of the applied computational method and may be explained by several contributing factors.

In a previous study, we demonstrated that including explicit solvent molecules can affect the nuclear conformations visited by the MD simulations, thereby influencing the injection rate in for specific dye molecules.[21] The absence of explicit solvation in the simulations increases the P1 flexibility, thereby enhancing the non-adiabatic coupling between donor and acceptor states, accelerating the decay process. Recent studies on photoinduced intramolecular charge transfer dynamics in a ruthenium-based chromophore have shown that explicitly accounting for solvent molecules can considerably slow down electron and hole mobility due to solute-solvent polarization effects.[26] Neglecting such polarization effects in our simulations could therefore lead to an overly fast injection process. Finally, our model system shows a fast and isotropic diffusion of the hole wave

packet into the NiO slab, whereas the actual injection process is constrained by the anti-ferromagnetically coupled spin layers in the NiO (111) plane. Again, this approximation could contribute to the slightly faster injection in the model system compared to the TA measurements.

Both the TA measurements and the quantum-classical dynamics simulations highlight the importance of nuclear motion for the injection process. Our results support the idea that the increase in solvent viscosity is the underlying reason for the higher $\tau_2$-$\tau_5$ in $H_2O$ + PEG compared to $H_2O$. We note here that the very small change in solvent reorganization energy due to a change in solvent polarity in the presence of PEG might also decrease the electron transfer rate according to Marcus theory. However, this slight change in polarity is not expected to play a role on the sub-ps timescales at which the solvent has not yet adjusted to the electronic excitation and the system is out of equilibrium.

The performed quantum-classical dynamics simulations of the dye standing perpendicular to the surface reveal that the removal of nuclear motion doubles the injection time scale ($\tau$ = 374 fs for simulations on moving nuclei *vs.* $\tau$ = 760 fs for a simulations on a static structure), and that the hole transfer stagnates after *ca.* 69 % injection. Fourier analysis of the hole-transfer simulations on moving nuclei reveals that the spectrum of the injection trace is characterized by frequencies in the 0-1700 $cm^{-1}$ range. In contrast, the injection on fixed nuclei is characterized by much higher frequencies, around 6000 $cm^{-1}$ and above 12000 $cm^{-1}$. It thus appears that the hole dynamics are affected considerably by the nuclear motion of the dye. Specifically, torsional motions around the dihedral angles between the three aniline components in the P1 dye (see Figure 6.6g, green dihedrals), appear to be resonant with the hole density propagation. Prior to injection, the hole wave packet oscillates multiple times between the two P1 tails. We propose that a specific conformation involving the dihedrals between the core aniline units directs the hole wave packet either toward the opposite P1 tail, or toward the NiO surface. In addition to these dihedral angle torsions, also fluctuations in the Ni-O bond lengths at the NiO/P1 interface appear to correlate with the photoinduced

injection trace. Overall, the performed calculations underscore how the injection process is strongly coupled to nuclear motion of the dye. These findings align with the literature, where coupled electron-nuclear dynamics is a feature observed for charge transfer in molecules, materials and biological systems.[21,24–27,52–56]

## 6.6 Conclusions

In summary, we have performed quantum-classical dynamics simulations in combination with TA spectroscopy to investigate the effects of nuclear motion on the photoinduced hole injection dynamics at the prototype NiO/P1 photocathode interface. The injection process of the excited dye P1* into the NiO surface is best fitted with a biphasic exponential consisting of an ultrafast component ($\tau_1$ of 76 ± 3 ps, within the TA instrument response) and a slower component ($\tau_2$ of 479 ± 13 fs). Based on quantum chemical modeling, we assign the fast component to P1 molecules that are strongly coupled to NiO, possibly through π-stacking interactions of the P1 tails to the surface. The slow component is assigned to P1 molecules standing perpendicular to the surface. Notably, the lifetime of this slow component depends on the solvent viscosity, as was shown by comparing the TA data of the NiO/P1 system in water and in water with 4.5 wt% PEG. Also charge recombination is slightly slowed down in more viscous media.

Quantum-classical dynamics simulations show excellent agreement with the TA results and further highlight the critical role of nuclear motion. Simulations of quantum hole dynamics on moving nuclei predict an approximately two-fold faster injection rate compared to those on fixed nuclei. Subsequent frequency domain analysis shows that the fluctuations of the hole survival probability on the P1* are in resonance with the vibrational fingerprint of the dye molecule. Specifically, torsional degrees of freedom around the P1 tails appear to be correlated with the injection trace. These results provide detailed insights into the fundamental photochemistry at the NiO/P1 interface, offering valuable guidelines for the design of highly efficient dye-sensitized photocathodes.

## 6.7 References


[1] K. Fan, F. Li, L. Wang, Q. Daniel, E. Gabrielsson, L. Sun, *Phys. Chem. Chem. Phys.* **2014**, *16*, 25234–25240.

[2] F. Li, K. Fan, B. Xu, E. Gabrielsson, Q. Daniel, L. Li, L. Sun, *J. Am. Chem. Soc.* **2015**, *137*, 9153–9159.

[3] S. Wrede, H. Tian, *Phys. Chem. Chem. Phys.* **2020**, *22*, 13850–13861.

[4] R. J. Dillon, L. Alibabaei, T. J. Meyer, J. M. Papanikolas, *ACS Appl. Mater. Interfaces* **2017**, *9*, 26786–26796.

[5] K. Zhu, G. Mul, A. Huijser, *Chemical Physics Reviews* **2024**, *5*, 021305.

[6] L. Zhang, G. Boschloo, L. Hammarström, H. Tian, *Phys. Chem. Chem. Phys.* **2016**, *18*, 5080–5085.

[7] J. M. Gardner, M. Beyler, M. Karnahl, S. Tschierlei, S. Ott, L. Hammarström, *J. Am. Chem. Soc.* **2012**, *134*, 19322–19325.

[8] J. Föhlinger, S. Maji, A. Brown, E. Mijangos, S. Ott, L. Hammarström, *J. Phys. Chem. C* **2018**, *122*, 13902–13910.

[9] K. Zhu, S. K. Frehan, A. M. Jaros, D. B. O'Neill, J. P. Korterik, K. Wenderich, G. Mul, A. Huijser, *J. Phys. Chem. C* **2021**, *125*, 16049–16058.

[10] C. J. Wood, G. H. Summers, C. A. Clark, N. Kaeffer, M. Braeutigam, L. R. Carbone, L. D'Amario, K. Fan, Y. Farré, S. Narbey, F. Oswald, L. A. Stevens, C. D. J. Parmenter, M. W. Fay, A. La Torre, C. E. Snape, B. Dietzek, D. Dini, L. Hammarström, Y. Pellegrin, F. Odobel, L. Sun, V. Artero, E. A. Gibson, *Phys. Chem. Chem. Phys.* **2016**, *18*, 10727–10738.

[11] M. G. Gatty, S. Pullen, E. Sheibani, H. Tian, S. Ott, L. Hammarström, *Chem. Sci.* **2018**, *9*, 4983–4991.

[12] L. J. Antila, P. Ghamgosar, S. Maji, H. Tian, S. Ott, L. Hammarström, *ACS Energy Lett.* **2016**, *1*, 1106–1111.

[13] P. Qin, J. Wiberg, E. A. Gibson, M. Linder, L. Li, T. Brinck, A. Hagfeldt, B. Albinsson, L. Sun, *J. Phys. Chem. C* **2010**, *114*, 4738–4748.

[14] C. J. Wood, G. H. Summers, E. A. Gibson, *Chem. Commun.* **2015**, *51*, 3915–3918.

[15] G. H. Summers, J.-F. Lefebvre, F. A. Black, E. Stephen Davies, E. A. Gibson, T. Pullerits, C. J. Wood, K. Zidek, *Phys. Chem. Chem. Phys.* **2016**, *18*, 1059–1070.

[16] M. Gennari, F. Légalité, L. Zhang, Y. Pellegrin, E. Blart, J. Fortage, A. M. Brown, A. Deronzier, M.-N. Collomb, M. Boujtita, D. Jacquemin, L. Hammarström, F. Odobel, *J. Phys. Chem. Lett.* **2014**, *5*, 2254–2258.

[17] K. L. Materna, A. M. Beiler, A. Thapper, S. Ott, H. Tian, L. Hammarström, *ACS Appl. Mater. Interfaces* **2020**, *12*, 31372–31381.

[18] K. Zhu, S. K. Frehan, G. Mul, A. Huijser, *J. Am. Chem. Soc.* **2022**, *144*, 11010–11018.

[19] A. Torres, R. S. Oliboni, L. G. C. Rego, *J. Phys. Chem. Lett.* **2015**.

[20] S. G. Abuabara, L. G. C. Rego, V. S. Batista, *J. Am. Chem. Soc.* **2005**, *127*, 18234–18242.

[21] J. P. Menzel, A. Papadopoulos, J. Belić, H. J. M. de Groot, L. Visscher, F. Buda, *J. Phys. Chem. C* **2020**, *124*, 27965–27976.

[22] A. V. Akimov, R. Asahi, R. Jinnouchi, O. V. Prezhdo, *J. Am. Chem. Soc.* **2015**, *137*, 11517–11525.

[23] A. Monti, C. F. A. Negre, V. S. Batista, L. G. C. Rego, H. J. M. De Groot, F. Buda, *J. Phys. Chem. Lett.* **2015**, *6*, 2393–2398.

[24] J. D. Gaynor, A. Petrone, X. Li, M. Khalil, *J. Phys. Chem. Lett.* **2018**, *9*, 6289–6295.

[25] F. Perrella, X. Li, A. Petrone, N. Rega, *JACS Au* **2023**, *3*, 70–79.

[26] F. Perrella, A. Petrone, N. Rega, *J. Chem. Theory Comput.* **2023**, *19*, 626–639.

[27] E. Buttarazzi, F. Perrella, N. Rega, A. Petrone, *J. Chem. Theory Comput.* **2023**, *19*, 8751–8766.

[28] E. Benazzi, J. Mallows, G. H. Summers, F. A. Black, E. A. Gibson, *J. Mater. Chem. C* **2019**, *7*, 10409–10445.

[29] K. Zhu, A. P. Rodríguez, M. B. Brands, T. De Haas, F. Buda, J. N. H. Reek, G. Mul, A. Huijser, *Adv. Sci.* **2024**, 2403454.
[30] S. Grimme, C. Bannwarth, P. Shushkov, *J. Chem. Theory Comput.* **2017**, *13*, 1989–2009.
[31] L. G. C. Rego, V. S. Batista, *J. Am. Chem. Soc.* **2003**, *125*, 7989–7997.
[32] R. Da Silva, D. A. Hoff, L. G. C. Rego, *J. Phys.: Condens. Matter* **2015**, *27*, 134206.
[33] A. B. Muñoz-García, M. Pavone, *Phys. Chem. Chem. Phys.* **2015**, *17*, 12238–12246.
[34] M. Wykes, F. Odobel, C. Adamo, I. Ciofini, F. Labat, *J. Mol. Model.* **2016**, *22*, 289.
[35] M. Alsabet, M. Grdeń, G. Jerkiewicz, *Electrocatalysis* **2015**, *6*, 60–71.
[36] V. Maffeis, B. Jousselme, T. Gustavsson, *Photochem. Photobiol. Sci.* **2021**, *20*, 1257–1271.
[37] L. D'Amario, J. Föhlinger, G. Boschloo, L. Hammarström, *Chem. Sci.* **2018**, *9*, 223–230.
[38] J. J. Snellenburg, S. P. Laptenok, R. Seger, K. M. Mullen, I. H. M. V. Stokkum, *J. Stat. Soft.* **2012**, *49*, 1-22.
[39] R. Hoffmann, *J. Chem. Phys.* **1963**, *39*, 1397–1412.
[40] J. H. Ammeter, H. B. Buergi, J. C. Thibeault, R. Hoffmann, *J. Am. Chem. Soc.* **1978**, *100*, 3686–3692.
[41] Alvarez, S. Table of Parameters for Extended Huckel Calculations. Universitat de Barcelona: Barcelona, 1993.
[42] F. Odobel, L. Le Pleux, Y. Pellegrin, E. Blart, *Acc. Chem. Res.* **2010**, *43*, 1063–1071.
[43] J. He, H. Lindstro, S.-E. Lindquist, *Sol. Energy Mater.* **2000**.
[44] L. Zhu, H. Yang, C. Zhong, C. M. Li, *Chem. Asian J.* **2012**, *7*, 2791–2795.
[45] D. Adler, J. Feinleib, *Phys. Rev. B* **1970**, *2*, 3112–3134.
[46] H. Sato, T. Minami, S. Takata, T. Yamada, *Thin Solid Films* **1993**, *236*, 27–31.
[47] E. L. Miller, R. E. Rocheleau, *J. Electrochem. Soc.* **1997**, *144*, 1995–2003.
[48] G. A. Sawatzky, J. W. Allen, *Phys. Rev. Lett.* **1984**, *53*, 2339–2342.
[49] E. Z. Kurmaev, R. G. Wilks, A. Moewes, L. D. Finkelstein, S. N. Shamin, J. Kuneš, *Phys. Rev. B* **2008**, *77*, 165127.
[50] C. Rödl, F. Fuchs, J. Furthmüller, F. Bechstedt, *Phys. Rev. B* **2009**, *79*, 235114.
[51] T. de Haas, K. Zhu, Y. Luo, G. Mul, F. Buda, A. Huijser **2025**, *J. Phys. Chem. C*. **2025**, *129* (14), 6817-6826.
[52] Y. Yoneda, S. J. Mora, J. Shee, B. L. Wadsworth, E. A. Arsenault, D. Hait, G. Kodis, D. Gust, G. F. Moore, A. L. Moore, M. Head-Gordon, T. A. Moore, G. R. Fleming, *J. Am. Chem. Soc.* **2021**, *143*, 3104–3112.
[53] P. You, D. Chen, X. Liu, C. Zhang, A. Selloni, S. Meng, *Nat. Mater.* **2024**, *23*, 1100–1106.
[54] R. L. Purchase, H. J. M. De Groot, *Interface Focus* **2015**, *5*, 1–16.
[55] X. Li, F. Buda, H. J. M. De Groot, G. J. Agur. Sevink, *J. Phys. Chem. C* **2019**, *123*, 16462–16478.
[56] X. Li, F. Buda, H. J. M. De Groot, G. J. A. Sevink, *J. Phys. Chem. B.* **2020**, *124*, 4026–4035.

## 6A. Appendix

### 6A.1 Computational details on DFT-based NiO slab structure optimizations

All optimizations were carried out using the Quickstep module in the CP2K8.2 software package.[1] The calculations applied the generalized gradient approximation (GGA) introduced by Perdew, Burke and Ernzerhof for the treatment of the exchange correlation potential with Grimme's third generation of dispersion corrections including a 22 Å cutoff and grid-smoothening.[2–5] A Mullikan based Hubbard-U parameter of 3.4 eV was applied on the Ni d-electrons to improve the description of the electronic structure over the standard GGA based DFT. Details on the optimization of the Hubbard-U parameter are provided in A.5. The calculations employed a hybrid Gaussian Plane Wave (GPW) scheme as implemented in the Quickstep routine in CP2K8.2.[6] The Ni and O valence electrons were expanded in the DZVP-MOLOPT-SR-GTH basis, while the core-valence electron interactions were modeled with pseudopotentials developed by Goedecker, Teter and Hutter.[7–9] A cut-off energy of 400 Ry was used for the auxiliary plane wave basis. All calculations considered only the Γ-point. Optimizations of the electronic structure were converged to $5 \cdot 10^{-7}$ H cycle$^{-1}$ and geometric structure optimizations were converged to root mean square values of $10^{-4}$ Bohr$^{-1}$ in the step size and $10^{-5}$ H Bohr$^{-1}$ in the forces.

6A.2 NiO structure optimization.

The bulk structure of NiO was optimized in a rhombohedral cell ($\alpha=\beta=\gamma=60°$) containing 64 nickel and 64 oxygen atoms at the DFT+U level of theory in CP2K8.2.[1] Cell-optimizations yielded a quasi-perfect rock salt structure with an average cubic lattice parameter of 4.17 Å, which matches lattice parameters reported in literature.[10–12] Visualization of the spin-density demonstrates that the optimized electronic structure exhibits anti-ferromagnetic spin alignments in the (111) plane (see Figure 6A.1). The bulk optimized rhombohedral was transformed to an orthorhombic box and cut along the (100) direction. The *x* and *y* dimensions of the box where preserved, but the *z*-axis was elongated to 40.0 Å, introducing a vacuum of 28.2 Å above the surface. Subsequently, a structure optimization was

carried out in which the lowest layer of nickel and oxide atoms were kept at fixed positions to simulate the constraining effect of the bulk material. In line with previous studies, the (100) surface undergoes only minor rearrangements.[13–16] As a sanity check, slab optimizations were carried out also for the (111) surface. This yielded a structure that aligns with reports in literature.[17]

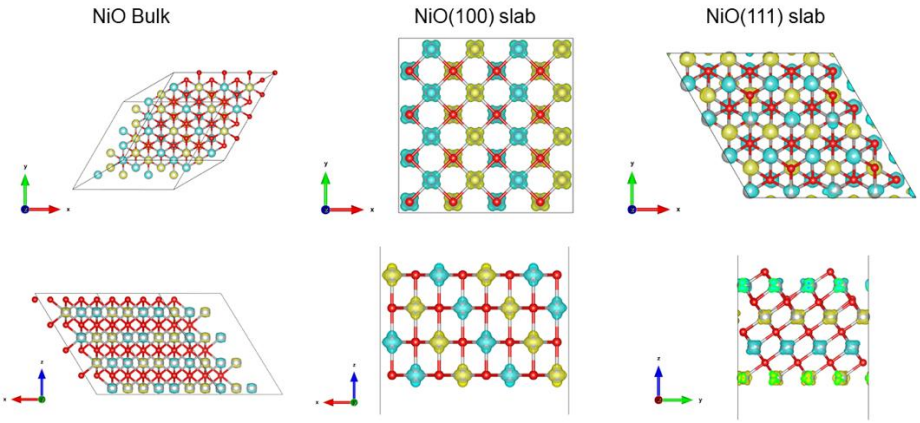


***Figure 6A.1****: Visualization of the DFT+U optimized bulk and slab NiO structures. Spin densities are plotted in yellow (spin up) and cyan (spin down). The spins are observed to align in the (111) plane for both phases, forming anti-ferromagnetically coupled sheets.*

### 6A.3 Ground state P1/NiO molecular dynamics simulations

The optimized NiO (100) surface slab was used to generate a 3-layer orthorhombic slab of 8 by 4 NiO units (192 Ni and 192 O atoms in total). In the center of the unit cell, the optimized P1 dye was attached to the surface through a bidentate binding mode where both carboxylate oxygens were attached to two distinct nickel atoms (see Figures 6A.2c and 6A.2d for a visualization of the system). Previous DFT studies of a similar dye with a carboxylate anchoring group have shown that this is the preferred binding mode on NiO (100).[16] Optimizations and

molecular dynamics (MD) simulations of the dye attached to the surface were subsequently performed at the GFN-xTB level of theory, including Grimme's third generation of pairwise additive dispersion corrections.[4] The P1 structure was optimized on the surface, and initial conditions for a production run were obtained by performing a 5 ps equilibration run at 300 K. The timestep for this equilibration run was set to 0.5 fs and a constant temperature was maintained with the Canonical Sampling through Velocity Rescaling (CSVR) thermostat.[18] The timestep for the production runs was set to 0.1 fs. During the optimization, equilibration and production runs, the positions of the nickel and oxygen atoms of the NiO slab were kept fixed. We note that we have also attempted MD simulations with fully relaxed Ni and O atoms. However, we found that NiO rock salt structure was unstable during these simulations, resulting in nickel and oxygen dissociation from the surface. These unstable dynamics are likely a result of the limitations of GFN-xTB in properly describing the anti-ferromagnetically coupled spin layers in the NiO (111) plane. To validate the decision to neglect structural relaxations of NiO in response to the P1 dye anchoring, DFT-based MD simulations were performed on a small representative model system. This system consisted of a 4-(diphenylamino)benzoic acid molecule on a NiO (100) slab of four layers of 8x8 NiO units and explicit water solvation. The simulation showed that neither the solvent nor the dye molecule had significant effects on the NiO surface structure, justifying the approach described above. The DFT-based simulations on the small model are further discussed in A.6.

### 6A.4 Electron and hole wavepacket simulations

After the ground states nuclear trajectories were obtained, the evolution of the excited states electron and hole wave packets were simulated on the basis of the Extended Hückel formalism, as implemented in the DynEMol software.[19] For all simulations, the photoexcited state was prepared by initiating an electron wave packet in the P1 LUMO and a hole wave packet in the P1 HOMO, which is justifiable considering that the 0-0 excitation in the P1 dye is largely dominated

by the HOMO-LUMO transition (see A.7). The time-step for the wave packet propagation was set to 0.1 fs, which is short enough to guarantee proper convergence of the electronic sub-system.[20] The quantum propagation of the wave packet is followed by calculating the time-dependent survival probability (SP) on the dye and on the NiO slab. This property is calculated by projecting the wave function at time $t$, on the atomic orbital basis of the molecular sub-system of interest.[21]

### 6A.5 Optimization of the Hubbard-U parameter

As mentioned in the section 6A.1.2, the calculations reported in the paper employed a Mulliken-based Hubbard U parameter of 3.4 eV to the Ni d-electrons to improve the description of the NiO electronic structure over standard GGA-DFT. As the goal of the DFT optimizations was only to obtain a structure for the subsequent quantum wave packet simulations, we focused on obtaining a correct geometry rather than reproducing an accurate band gap. With these considerations in mind, a series of 6 bulk phase cell-optimizations were performed, applying a Hubbard parameter of 1, 2, 3, 4, 5 or 6 eV, respectively. These cell-optimizations were performed on a rhombohedral box containing 64 nickel and 64 oxygen atoms. This series was later extended with additional optimizations applying a U parameter of 3.4 and 3.6 eV. Subsequently, a series of electronic structure optimizations was performed on a perfect NiO bulk structure with a lattice parameter of 4.17 Å, to extract the predicted band gap. The obtained lattice parameter and band gap energies are provided in Table 6A.1. Based on these benchmark calculations, it was decided to perform the slab optimizations with a Hubbard U parameter of 3.4 eV, as this yielded a good compromise between the predicted lattice parameter and band gap properties.

**Table 6A.1**. Lattice parameters and band gap energies for the performed NiO bulk phase optimizations with different Hubbard U values. Experimental data are shown in the last column.

| *Hubbard U parameter (eV)* | 1 | 2 | 3 | 3.4 | 3.6 | 4 | 5 | 6 | *Exp.* |
|---|---|---|---|---|---|---|---|---|---|
| *Lattice parameter (Å)* | 4.12 | 4.18 | 4.17 | 4.16 | 4.15 | 4.18 | 4.15 | 4.10 | 4.17[10–12] |
| *Band Gap (eV)* | 1.48 | 1.64 | 1.93 | 2.10 | 2.19 | 2.39 | 2.90 | 2.75 | 3.4-4.0 |

## 6A.6 DFT-based molecular dynamics of a model dye-NiO system in explicit solvation

To investigate the structural response of the NiO surface to the anchoring of P1, DFT-based molecular dynamics were performed using a small model system. In this model system, P1 was represented by a 4-(diphenylamino)benzoic acid (4DPABA) molecule. 4DPABA represents a good model for the P1 dye as it contains the same benzoic acid anchoring group and triphenyl amine core. The same computational settings were employed as described in section 6A.1 The optimized NiO (100) surface was used to generate a slab of 4 layers of 4 by 4 NiO units (total of 128 Ni and 128 O atoms). The 4DPABA molecule was considered to attach to the surface in a bidentate binding mode, as earlier studies from Pavone *et al* have shown that this is energetically more stable than the monodentate binding.[16] The carboxylate oxygen atoms were considered to bind to two distinct Ni atoms at the surface, while the dissociating carboxylate proton was considered to bind to the adjacent oxygen atom. Since each Ni atom hosts two unpaired electrons, two distinct binding modes are possible: one in which the two carboxylate oxygen atoms bind to two Ni atoms with the same spin polarization ($\alpha\alpha$-binding), and another where they bind to two Ni atoms with opposite spin polarization ($\alpha\beta$-binding). Furthermore, we considered two different surface species. The first species stands perpendicular to the NiO surface and is displayed in Figure 6A.2a, while the second species lies flat on the surface and is displayed in Figure 6A.2b. All interface structures were optimized in a cubic box with

dimensions 16.6 by 16.6 by 24 Å. The energies associated with each species are reported in Table 6A.2. Interestingly, the species were the 4DPABA dye lies flat on the surface was found to be ~30 kcal mol$^{-1}$ lower in energy than the species where the dye stands perpendicular to the surface. The difference between binding two to nickel atoms of same or opposite spin appears to have an effect in the order of 1 kcal mol$^{-1}$.

**Table 6A.2**. Relative energies for the four considered 4DPABA surface species.

| | Energy (kcal mol$^{-1}$) |
|---|---|
| *standing perpendicular (αα)* | 30.4 |
| *standing perpendicular (αβ)* | 29.3 |
| *flat on surface (αα)* | 0 |
| *flat on surface (αβ)* | 0.9 |

After geometry optimizations of the 4DPABA-NiO interface, 129 water molecules were added to the simulation box with the PACKMOL builder tool as implemented in AMS2021.[22,23] The system was equilibrated for 1 ps, and subsequently propagated for another 3 ps at the DFT-MD level. During the dynamics, the CSVR thermostat was applied with a timestep of 50 fs.[18] Figure 6A.2c-d presents a snapshot from the MD simulations. During the dynamics, the 4DPABA dye was found to remain strictly perpendicular to the surface and the bidentate binding mode was found to remain stable for the entire duration of the simulation. This indicates that the interconversion between the conformations - with the dye standing perpendicular or parallel to the surface - is associated with a barrier substantially higher than $k_B$T. Water molecules appeared to be strongly physisorbed to the surface, with the oxygen atoms consistently oriented towards the surface nickel atoms, while the hydrogens atoms formed strong hydrogen bonds with the surface oxygen atoms. During the course of the simulation, two water molecules underwent O-H bond dissociation, resulting in their

chemisorption on the surface. The binding of the 4DPABA molecule has a limited effect on the structure or the dynamics of the Ni and O atoms at the dye-surface interface. This result justifies the assumption of neglecting the structural motion within the NiO slab in the GFN-xTB simulations reported in the main manuscript.

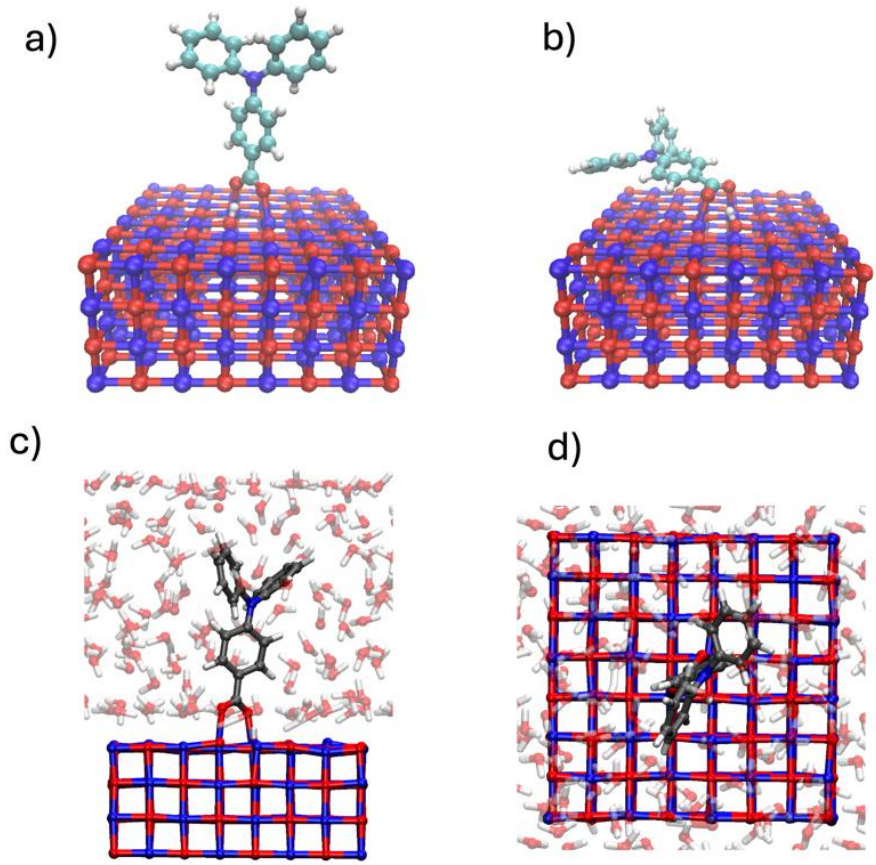


***Figure 6A.2**. a) and b) present visualizations of the 4DPABA dye in perpendicular orientation towards to surface and in when it lies on the surface, respectively. Top (c) and side (d) view of snapshots from the DFT-based molecular dynamics simulations of 4DPABA on NiO.*

### 6A.7 DFT optimization and TDDFT excitations spectrum of the P1 dye

The P1 geometry was optimized at the DFT level using the AMS2021 program.[23] The optimizations employed the hybrid B3LYP exchange-correlations functional in an all-electron, triple-ζ (TZP) Slater-type basis. Van der Waals forces were corrected by the third generation of Grimme's dispersion corrections including Becke and Johnsen damping functions (D3BJ),[3–5,24] and relativistic effects were included by means of the Zeroth Order Regular Approximation (ZORA).[25] The COnductor like Screening MOdel (COSMO) was employed to take into account the electronic polarization effects of the water environment.[26–28] The numerical integration was improved over the default setting to "good", and the self-consistent field convergence was tightened to $10^{-8}$ H. A frequency calculation on the optimized P1 geometry did not reveal any imaginary eigenmodes, thereby verifying that the obtained structure represents a local minimum on the potential energy surface. The excitation spectrum was calculated by a Time-Dependent DFT (TDDFT) calculation within the Tamm-Dancoff formalism, employing the same settings as described above.[29]

The lowest 5 electronic excitations calculated by TDDFT are provided in Table 6A.3. According to this calculation at the B3LYP level, the first bright (oscillator strength of 1.51 a.u.) excitation is largely (98.7%) described by the HOMO-LUMO transition.

**Table 6A.3**. Unrestricted TDDFT (B3LYP-D3BJ/TZP) excitation spectrum of the P1 dye in implicit water solvation (COSMO). Also the first spin-forbidden singlet-triplet excitations are included.

| | Spin | Excitation energy (eV) | Oscillator strength (a.u.) | Major MO contributions |
|---|---|---|---|---|
| 1 | singlet-triplet | 1.73 | 0.05 | α:156 →157 (53%), β:156 →157 (26%) |
| 2 | singlet-triplet | 1.80 | 0.00 | α:156 →158 (48%), β:156 →157 (22%) |
| 3 | singlet-singlet | 2.15 | 1.51 | β:156 →157 (64%) α:156 →157 (35%) |
| 4 | singlet-singlet | 2.35 | 0.20 | β:156 →158 (67%) α:156 →158 (29%) |
| 5 | singlet-triplet | 2.42 | 0.01 | α:155 →157 (30%), α:156 →158 (19%), β:155 →157 (17%), α:154 →158 (12%) |

### 6A.8 Optimization of the Extended-Hückel parameters

The simulations of electron and hole wave packets described in this work were performed within the framework of Extend-Hückel (EH) theory. A more elaborate overview of this method is provided for instance in ref.[30] The EH calculations on the NiO-P1 interface using the default EH parameters[31] did not yield a driving force for the hole transfer from the excited P1* to the NiO surface. A realistic alignment of the P1 frontier orbitals with respect to the NiO valence band (VB), as well as a widening of the P1 HOMO-LUMO gap and a narrowing of the NiO band gap was achieved by fine-tuning the Coulomb integral parameters with a genetic algorithm. The optimization of the NiO parameters was performed on a bulk-phase, cubic NiO structure, containing 32 nickel and 32 oxygen atoms in a perfect rock-salt formation. Periodic boundary conditions were employed in the [100], [010] and [001] directions. The parameters for the P1 dye were optimized by performing the EH calculations on a DFT-optimized structure of the free P1 dye including the proton on the carboxylate group, that would later dissociate

upon anchoring to the NiO. During the optimization procedure, a distinction was made between different carbon and nitrogen atoms that were found in different chemical environments. A schematic representation of the different atomic species is provided in Figure 6A.3a. In each optimization run, the genetic algorithm spawned a population of 50 sets of parameters of which the 2 best performing sets were propagated to the next generation. After 10 generations, the best performing set of parameters was assessed by hand to see whether the relevant orbitals still preserved the correct symmetry and spatial distribution. The target values for the optimization procedure are given in Table 6A.4, while the formulation of the cost function is described in an earlier work.[30] Figure 6A.3b provides a visual comparison between the frontier P1 orbitals calculated with DFT and with the final EH parameters. The obtained EH parameters for all chemical elements, as described in Figure 6A.3a, are provided in the A.11 appendix.

**Table 6A.4**. The NiO VBM (valence band maximum), NiO CBM (conduction band minimum) and P1 energy level alignment with the original and optimized EH parameters.

| | P1 HOMO (eV) | P1 LUMO (eV) | NiO VBM (eV) | NiO CBM (eV) |
|---|---|---|---|---|
| Original parameters | –11.2 | –9.8 | –12.3 | –5.6 |
| Optimized parameters | –11.4 | –9.2 | –10.4 | –6.4 |
| Optimization targets | –11.4 | –9.2 | –10.5 | –6.5 |

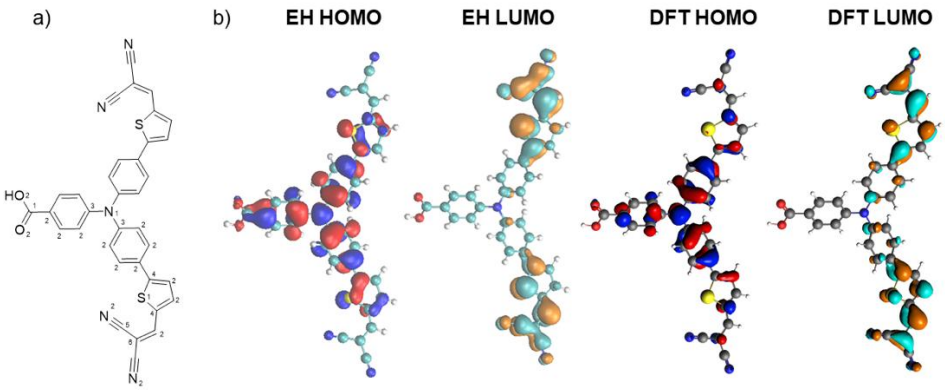


***Figure 6A.3****. a) provides the distinct atomic species in the EH optimization procedure. A visual comparison between the P1 HOMO and LUMO orbitals calculated at the DFT level and at the EH level is provided in b). The B3LYP functional was used for the DFT calculations*. Isosurfaces of the HOMO and LUMO orbitals were plotted at a density value of 0.03.

### 6A.9 Electron dynamics simulations on static structures and dynamics nuclear trajectories

Figure 6A.4 presents the electron survival probability on the excited P1* calculated from the quantum wave packet simulations on MD trajectories including nuclear motion (green) and static nuclear structures (red). The three different panels correspond to the three initial conditions sampled from the performed classical MD simulations at $t$=0 fs, $t$=1000 fs and $t$=2000 fs. The electron wave packet remains localized on the dye throughout all three wave packet simulations on the MD trajectories including thermal nuclear motion. In contrast, the simulations on static structures show a gradual electron transfer to the NiO slab after the initial ~200 fs of the simulation. This suggests that a recombination pathway becomes accessible, enabling coherent charge transfer from the P1 LUMO to the NiO valence band. Interestingly, nuclear motion

appears to quench this coherent transfer and prevents the recombination on the simulated timescale of 1 ps.

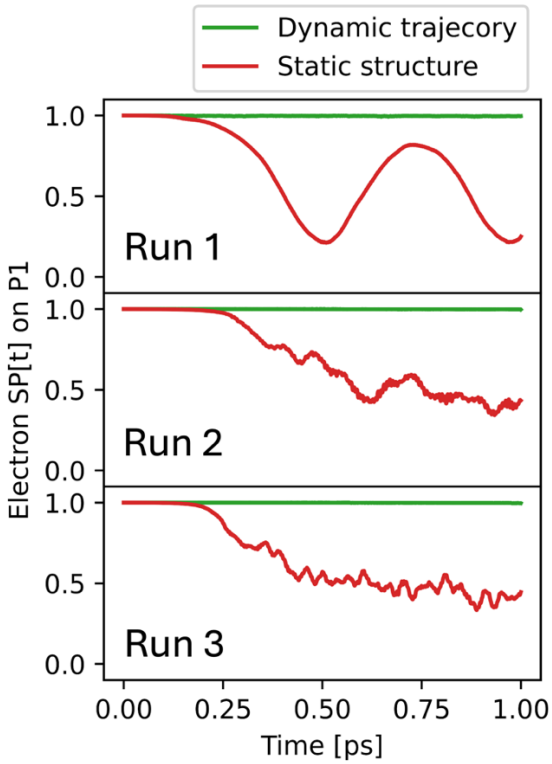


***Figure 6A.4**: Time-dependent electron survival probability on the P1 dye on the static nuclear structures (red) and dynamic nuclear trajectories (green).*

### 6A.10 Ordering of HOMO and HOMO–1 states for different conformations sampled from MD

Before performing the photoinduced hole injection quantum dynamics simulations, the relative alignment of the HOMO and HOMO–1 orbitals was investigated for a series of 30 different structures sampled from the MD simulations. For each of these structures, we performed two quantum dynamics simulations with the hole initialized in the HOMO or in the HOMO–1 orbital of the system. Subsequently, the hole density was visualized after the first 0.1 fs

timestep. The orbital energies are plotted in Figure 6A.5a, while two representative hole density visualizations are provided in Figure 6A.5b. It was observed that for several conformational structures the HOMO and HOMO–1 orbitals become nearly degenerate and that for four structures their relative alignment is reversed.

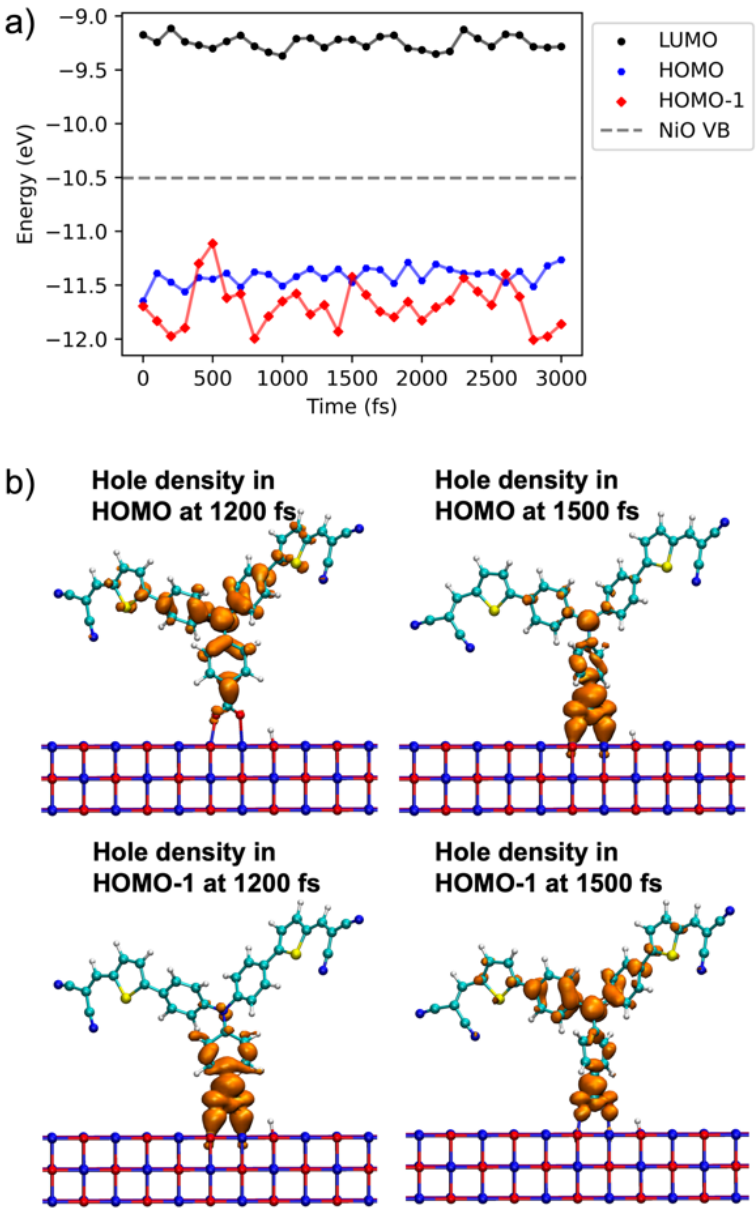


***Figure 6A.5.*** *a) The energies of the LUMO, HOMO and HOMO–1 states in the 3 ps time interval. b) Visualizations of the hole wave packet density initiated in the HOMO and HOMO–1 states at 1200 fs and 1500 fs. At this stage, the order of the energy levels is reversed, and the two states are mixed.*

## 6A.11 Extended Hückel-based DOS plot for P1 lying flat on surface

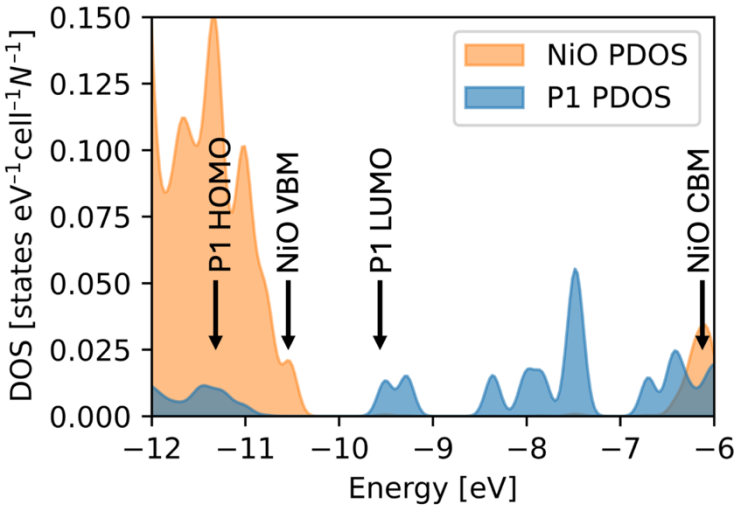


***Figure 6A.6.*** *Plot of the electronic density of states (DOS) of the optimized P1 dye on lying flat on the NiO (100) slab (Species 2, Figure 6.4b).*

## 6A.11: The optimized EH parameters

| Symbol | MMsymbol | NoAt | Nvalen | Nzeta | n | spdf | IP | zeta1 | zeta2 | coef1 | coef2 | k_WH |
|---|---|---|---|---|---|---|---|---|---|---|---|---|
| O | O1 | 8 | 6 | 1 | 2 | s | -31.97708 | 2.419349 | 0.000000 | 1.000000 | 0.000000 | 2.388173 |
| O | O1 | 8 | 6 | 1 | 2 | p | -12.44601 | 2.188920 | 0.000000 | 1.000000 | 0.000000 | 1.708553 |
| Ni | Ni1 | 28 | 10 | 1 | 4 | s | -8.35691 | 2.423005 | 0.000000 | 1.000000 | 0.000000 | 1.726895 |
| Ni | Ni1 | 28 | 10 | 1 | 4 | p | -5.04010 | 1.550887 | 0.000000 | 1.000000 | 0.000000 | 3.040000 |
| Ni | Ni1 | 28 | 10 | 2 | 3 | d | -12.95211 | 5.881614 | 2.300000 | 0.568300 | 0.629200 | 2.007307 |
| C | C1 | 6 | 4 | 1 | 2 | s | -21.83998 | 1.502273 | 0.000000 | 1.000000 | 0.000000 | 1.652710 |
| C | C1 | 6 | 4 | 1 | 2 | p | -11.11776 | 1.578776 | 0.000000 | 1.000000 | 0.000000 | 1.271570 |
| C | C2 | 6 | 4 | 1 | 2 | s | -21.64263 | 1.392992 | 0.000000 | 1.000000 | 0.000000 | 1.586950 |
| C | C2 | 6 | 4 | 1 | 2 | p | -11.30164 | 1.592068 | 0.000000 | 1.000000 | 0.000000 | 2.189580 |
| C | C3 | 6 | 4 | 1 | 2 | s | -21.30227 | 1.602251 | 0.000000 | 1.000000 | 0.000000 | 1.399880 |
| C | C3 | 6 | 4 | 1 | 2 | p | -12.56206 | 1.907199 | 0.000000 | 1.000000 | 0.000000 | 1.909580 |
| C | C4 | 6 | 4 | 1 | 2 | s | -21.26181 | 1.652660 | 0.000000 | 1.000000 | 0.000000 | 1.905050 |
| C | C4 | 6 | 4 | 1 | 2 | p | -11.55636 | 1.727973 | 0.000000 | 1.000000 | 0.000000 | 1.932090 |
| C | C5 | 6 | 4 | 1 | 2 | s | -21.79423 | 1.641574 | 0.000000 | 1.000000 | 0.000000 | 1.521610 |
| C | C5 | 6 | 4 | 1 | 2 | p | -10.69162 | 1.507971 | 0.000000 | 1.000000 | 0.000000 | 2.166900 |
| C | C6 | 6 | 4 | 1 | 2 | s | -21.66886 | 1.537034 | 0.000000 | 1.000000 | 0.000000 | 1.718590 |
| C | C6 | 6 | 4 | 1 | 2 | p | -11.56014 | 1.599292 | 0.000000 | 1.000000 | 0.000000 | 1.678440 |
| S | S1 | 16 | 6 | 1 | 3 | s | -20.14530 | 2.069794 | 0.000000 | 1.000000 | 0.000000 | 2.032820 |
| S | S1 | 16 | 6 | 1 | 3 | p | -11.89877 | 1.899772 | 0.000000 | 1.000000 | 0.000000 | 3.837720 |
| N | N1 | 7 | 5 | 1 | 2 | s | -25.46722 | 2.010008 | 0.000000 | 1.000000 | 0.000000 | 1.282550 |
| N | N1 | 7 | 5 | 1 | 2 | p | -12.73100 | 2.281318 | 0.000000 | 1.000000 | 0.000000 | 1.988070 |
| N | N2 | 7 | 5 | 1 | 2 | s | -26.01483 | 1.859309 | 0.000000 | 1.000000 | 0.000000 | 1.817200 |
| N | N2 | 7 | 5 | 1 | 2 | p | -13.46475 | 2.227766 | 0.000000 | 1.000000 | 0.000000 | 1.427180 |
| O | O2 | 8 | 6 | 1 | 2 | s | -32.51769 | 1.823570 | 0.000000 | 1.000000 | 0.000000 | 1.869520 |
| O | O2 | 8 | 6 | 1 | 2 | p | -14.66009 | 1.962404 | 0.000000 | 1.000000 | 0.000000 | 2.132110 |

## 6A.12 References


[1] T. D. Kühne, M. Iannuzzi, M. Del Ben, V. V. Rybkin, P. Seewald, F. Stein, T. Laino, R. Z. Khaliullin, O. Schütt, F. Schiffmann, D. Golze, J. Wilhelm, S. Chulkov, M. H. Bani-Hashemian, V. Weber, U. Borštnik, M. Taillefumier, A. S. Jakobovits, A. Lazzaro, H. Pabst, T. Müller, R. Schade, M. Guidon, S. Andermatt, N. Holmberg, G. K. Schenter, A. Hehn, A. Bussy, F. Belleflamme, G. Tabacchi, A. Glöß, M. Lass, I. Bethune, C. J. Mundy, C. Plessl, M. Watkins, J. VandeVondele, M. Krack, J. Hutter, *J. Chem. Phys.* **2020**, *152*, 194103.

[2] J. P. Perdew, K. Burke, M. Ernzerhof, *Phys. Rev. Lett.* **1997**, *78*, 1396–1396.

[3] S. Grimme, *J. Comput. Chem.* **2004**, *25*, 1463–1473.

[4] S. Grimme, *Wiley Interdiscip. Rev. Comput. Mol. Sci.* **2011**, *1*, 211–228.

[5] S. Grimme, *Chemistry - Chem. - Eur. J.* **2012**, *18*, 9955–9964.

[6] J. VandeVondele, M. Krack, F. Mohamed, M. Parrinello, T. Chassaing, J. Hutter, *Comput. Phys. Commun.* **2005**, *167*, 103–128.

[7] S. Goedecker, M. Teter, J. Hutter, *Phys. Rev. B* **1996**, *54*, 1703–1710.

[8] C. Hartwigsen, S. Goedecker, J. Hutter, *Phys. Rev. B* **1998**, *58*, 3641–3662.

[9] M. Krack, *Theor. Chem. Acc.* **2005**, *114*, 145–152.

[10] R. W. Cairns, E. Ott, *J. Am. Chem. Soc.* **1933**, *55*, 527–533.

[11] A. K. Cheetham, D. A. O. Hope, *Phys. Rev. B* **1983**, *27*, 6964–6967.

[12] B. Walls, A. A. Mazilkin, B. O. Mukhamedov, A. Ionov, I. A. Smirnova, A. V. Ponomareva, K. Fleischer, N. A. Kozlovskaya, D. A. Shulyatev, I. A. Abrikosov, I. V. Shvets, S. I. Bozhko, *Sci. Rep.* **2021**, *11*, 3496.

[13] S. Piccinin, D. Rocca, M. Pastore, *J. Phys. Chem. C* **2017**, *121*, 22286–22294.

[14] A. Segalina, S. Lebègue, D. Rocca, S. Piccinin, M. Pastore, *J. Chem. Theory Comput.* **2021**, *17*, 5225–5238.

[15] J. Massin, M. Bräutigam, S. Bold, M. Wächtler, M. Pavone, A. B. Muñoz-García, B. Dietzek, V. Artero, M. Chavarot-Kerlidou, *J. Phys. Chem. C* **2019**, *123*, 17176–17184.

[16] A. B. Muñoz-García, M. Pavone, *Phys. Chem. Chem. Phys.* **2015**, *17*, 12238–12246.

[17] W. Zhao, A. D. Doyle, S. E. Morgan, M. Bajdich, J. K. Nørskov, C. T. Campbell, *J. Phys. Chem. C* **2017**, *121*, 28001–28006.

[18] G. Bussi, D. Donadio, M. Parrinello, *J. Chem. Phys.* **2007**, *126*, 014101.

[19] A. Torres, R. S. Oliboni, L. G. C. Rego, *J. Phys. Chem. Lett.* **2015**.

[20] R. Da Silva, D. A. Hoff, L. G. C. Rego, *J. Phys.: Condens. Matter* **2015**, *27*, 134206.

[21] L. G. C. Rego, V. S. Batista, *J. Am. Chem. Soc.* **2003**, *125*, 7989–7997.

[22] L. Martínez, R. Andrade, E. G. Birgin, J. M. Martínez, *J. Comput. Chem.* **2009**, *30*, 2157–2164.

[23] AMS2022.101, Theoretical Chemistry, VrijeUniversiteit, Amsterdam, The Netherlands 2022, https://www.scm.com.

[24] S. Grimme, S. Ehrlich, L. Goerigk, *J. Comput. Chem.* **2011**, *32*, 1456–1465.

[25] E. Van Lenthe, *J. Chem. Phys.* **1999**, *110*, 8943–8953.

[26] A. Klamt, *J. Phys. Chem.* **1995**, *99*, 2224–2235.

[27] A. Klamt, V. Jonas, *J. Chem. Phys.* **1996**, *105*, 9972–9981.

[28] C. C. Pye, T. Ziegler, E. Van Lenthe, J. N. Louwen, *Can. J. Chem* **2009**, *87*, 790–797.

[29] S. Hirata, M. Head-Gordon, *Chem. Phys. Lett.* **1999**, *314*, 291–299.

[30] A. Monti, C. F. A. Negre, V. S. Batista, L. G. C. Rego, H. J. M. De Groot, F. Buda, *J. Phys. Chem. Lett.* **2015**, *6*, 2393–2398.

[31] Santiago Alvarez. Table of Parameters for Extended Hückel Calculations', Universitat de Barcelona: Barcelona, 1993

.